

CONSTRAINING PARAMETERS IN PULSAR MODELS OF REPEATING FRB 121102 WITH HIGH-ENERGY FOLLOW-UP OBSERVATIONS

DI XIAO^{1,2} AND ZI-GAO DAI^{1,2}

¹School of Astronomy and Space Science, Nanjing University, Nanjing 210093, China; dzg@nju.edu.cn and
²Key Laboratory of Modern Astronomy and Astrophysics (Nanjing University), Ministry of Education, China

Draft version November 8, 2018

ABSTRACT

Recently, a precise (sub-arcsecond) localization of the repeating fast radio burst (FRB) 121102 has led to the discovery of persistent radio and optical counterparts, the identification of a host dwarf galaxy at a redshift of $z = 0.193$, and several campaigns of searches for higher-frequency counterparts, which gave only upper limits on the emission flux. Although the origin of FRBs remains unknown, most of the existing theoretical models are associated with pulsars, or more specifically, magnetars. In this paper, we explore persistent high-energy emission from a rapidly rotating highly magnetized pulsar associated with FRB 121102 if internal gradual magnetic dissipation occurs in the pulsar wind. We find that the efficiency of converting the spin-down luminosity to the high-energy (e.g., X-ray) luminosity is generally much smaller than unity, even for a millisecond magnetar. This provides an explanation for the non-detection of high-energy counterparts to FRB 121102. We further constrain the spin period and surface magnetic field strength of the pulsar with the current high-energy observations. In addition, we compare our results with the constraints given by the other methods in previous works and would expect to apply our new method to some other open issues in the future.

Subject headings: pulsars: general – radiation mechanisms: non-thermal – stars: neutron

1. INTRODUCTION

The origin of fast radio bursts (FRBs) has been under intense debate since their discovery ten years ago (Lorimer et al. 2007; Keane et al. 2012; Thornton et al. 2013; Burke-Spolaor & Bannister 2014; Spitler et al. 2014, 2016; Champion et al. 2015; Masui et al. 2015; Petroff et al. 2015; Ravi et al. 2016; Caleb et al. 2017). Most of the 23 FRBs detected so far appear to be non-repeating, and various origin models for these kind of events have been proposed, such as collapse of supra-massive neutron stars to black holes (Falcke & Rezzolla 2014; Zhang 2014), mergers of binary white dwarfs (Kashiyama et al. 2013) or binary neutron stars (Totani 2013; Wang et al. 2016), or charged black holes (Liu et al. 2016; Zhang 2016), and so on (for a review of observations and physical models see Katz 2016a).

However, the discovery of the only repeating FRB 121102 shed new light on its origin, since the catastrophic event scenarios are not suitable for it (Spitler et al. 2016). The non-catastrophic models include giant flares from a magnetar (Popov & Postnov 2013; Kulkarni et al. 2014; Katz 2016b),¹ giant pulses from a young pulsar (Connor et al. 2016; Cordes & Wasserman 2016; Lyutikov et al. 2016), pulsar lightning (Katz 2017a), repeating collisions of a neutron star, an asteroid belt around another star (Dai et al. 2016; Bagchi 2017), and accretion in a neutron star-white dwarf binary (Gu et al. 2016). Among these models, a rapidly rotating highly magnetized neutron star is the astrophysical object

referred to most frequently. Moreover, the properties of the host dwarf galaxy of FRB 121102, which are consistent with those of long-duration gamma-ray bursts (GRBs) and hydrogen-poor superluminous supernovae (SLSNe), suggest the possibility that the repeating bursts originate from a young millisecond magnetar (Metzger et al. 2017). This possibility is further supported by the location of FRB 121102 within a bright star-forming region (Bassa et al. 2017). In addition, based on the recently discovered persistent radio source associated with FRB 121102 and the redshift of the host galaxy (Chatterjee et al. 2017; Marcote et al. 2017; Tendulkar et al. 2017), some constraints on the pulsar were widely discussed (e.g. Beloborodov 2017; Cao et al. 2017; Dai et al. 2017; Kashiyama & Murase 2017; Lyutikov 2017), but they were relaxed under the assumption that FRBs are wandering narrow beams (Katz 2017b). To our knowledge, in addition to FRBs, a pulsar can exhibit some observational signals in other wavelengths. Thus, searching for high-energy counterparts to FRB 121102 will possibly give us some hints about the central pulsar.

A pulsar is likely to generate an ultra-relativistic wind, and there are some observational signatures for such a wind. The measured radio spectrum of the Crab Nebula is naturally explained if a wind with a Lorentz factor of $\sim 10^4$ from the Crab pulsar is introduced (e.g. Atoyan 1999). The wind from a rapidly rotating highly magnetized pulsar is expected to be Poynting-flux-dominated (Coroniti 1990; Spruit et al. 2001) or alternatively turns into electron-positron pairs dominated above a certain radius, and then, even powering a GRB afterglow is possible (e.g. Dai & Lu 1998a,b; Dai 2004; Ciolfi & Siegel 2015; Rezzolla & Kumar 2015). The gradual dissipation of magnetic energy via reconnection is able to accelerate electrons and then

¹ Although this model is challenged by the non-detection of an expected bright radio burst during the 2004 December 27 giant gamma-ray flare of the Galactic magnetar SGR 1806-20, it is still possible to reconcile the theory with observations (Tendulkar et al. 2016).

produce radiation (Spruit et al. 2001; Drenkhahn 2002; Drenkhahn & Spruit 2002; Giannios & Spruit 2005; Giannios 2006, 2008; Metzger et al. 2011; Giannios 2012; Sironi & Spitkovsky 2014; Beniamini 2014; Kagan et al. 2015; Sironi et al. 2015).² Recently, Beniamini & Giannios (2017) found that this emission could be significant in the X-ray/gamma-ray band, which motivates us to constrain the parameters of the pulsar, especially its spin period and surface magnetic field strength, with the non-detection of high-energy counterparts to FRB 121102.

The observational results that we refer to mainly include three upper limits given by different instruments for different working bands, and are summarized below. A deep search for X-ray sources by *XMM-Newton/Chandra* placed a 5σ upper limit of 4.0×10^{-15} erg cm⁻² s⁻¹ on the 0.5 – 6 keV flux (Scholz et al. 2017). The 5σ flux upper limit by *Fermi-GBM* is 1.0×10^{-7} erg cm⁻² s⁻¹ (Scholz et al. 2016; Younes et al. 2016). In addition, an energy flux upper limit of 4.0×10^{-12} erg cm⁻² s⁻¹ was obtained over the eight-year span of *Fermi-LAT* (Zhang & Zhang 2017; Xi et al. 2017).

The paper is organized as follows. We introduce an internal gradual magnetic dissipation model (abbreviated as the IGMD model hereafter) of a wind from a rapidly rotating highly magnetized pulsar and predict an emission from the wind in Section 2. Then we calculate the radiation efficiency and constrain the spin period and surface magnetic field strength in Section 3. In Section 4 we provide a summary and compare with previous works, and also discuss an implication for future works.

2. EMISSION FROM A PULSAR WIND

An ultra-relativistic wind from a rapidly rotating highly magnetized pulsar is initially Poynting-flux-dominated (Coroniti 1990), and its magnetic energy can be converted to thermal emission and bulk kinetic energy of the wind via internal gradual magnetic dissipation due to reconnection in the IGMD model (Spruit et al. 2001; Drenkhahn 2002; Drenkhahn & Spruit 2002; Giannios & Spruit 2005). In addition, we also expect to observe non-thermal synchrotron emission from the electrons accelerated by magnetic reconnection (Beniamini 2014; Sironi & Spitkovsky 2014; Kagan et al. 2015). At a given radius, the Poynting-flux luminosity could be written as (Giannios & Spruit 2005; Beniamini & Giannios 2017)

$$L_B = c \frac{(rB)^2}{4\pi} = L_{\text{sd}} \left[1 - \frac{\Gamma(r)}{\Gamma_{\text{sat}}} \right], \quad (1)$$

where B and $\Gamma(r)$ are the magnetic field strength and Lorentz factor of the wind at radius r respectively. The energy injection luminosity of the wind is assumed to be the spin-down luminosity L_{sd} and Γ_{sat} is the bulk Lorentz factor of the wind at the saturation radius given by $r_{\text{sat}} = \lambda \Gamma_{\text{sat}}^2 / (6\epsilon) = 1.7 \times 10^{15} \Gamma_{\text{sat},4}^2 (\lambda/\epsilon)_8$ cm (Beniamini & Giannios 2017), where $\lambda \sim cP = 3 \times$

² This kind of gradual dissipation of magnetic energy via reconnection in these references is different from an abrupt and violent dissipation process arising from colliding shells in the internal-collision-induced magnetic reconnection and turbulence model proposed by Zhang & Yan (2011). This model can account for the main properties of GRBs themselves.

$10^7 P_{-3}$ cm is the wavelength of the magnetic field in the striped wind configuration (Coroniti 1990; Spruit et al. 2001; Drenkhahn 2002; Drenkhahn & Spruit 2002) and $\epsilon \sim 0.1 - 0.25$ is the ratio of reconnection velocity to the speed of light (Lyubarsky 2005; Guo et al. 2015; Liu et al. 2015). Throughout this work, we use the notation $Q = 10^x Q_x$ in cgs units. Since the comoving temperature decreases as $T' \propto r^{-7/9}$, the thermal luminosity decreases as $L_{\text{th}}(r) \propto r^{-4/9}$ (Giannios & Spruit 2005), substituting the energy dissipation rate $d\dot{E} = -(dL_B/dr)dr$; then the total thermal photospheric luminosity can be obtained by integrating from the initially launching radius to the photospheric radius r_{ph} (Giannios & Spruit 2005; Beniamini & Giannios 2017),

$$\begin{aligned} L_{\text{ph}} &= \int_0^{r_{\text{ph}}} \frac{1}{2} \left(\frac{r}{r_{\text{ph}}} \right)^{4/9} d\dot{E} \\ &= 2.6 \times 10^{47} L_{\text{sd},50}^{6/5} \Gamma_{\text{sat},4}^{-1} \left(\frac{\lambda}{\epsilon} \right)_8^{-1/5} \text{ erg s}^{-1} \text{ sr}^{-1}, \end{aligned} \quad (2)$$

with the temperature being³

$$T_{\text{ph}} = 95 L_{\text{sd},50}^{1/10} \Gamma_{\text{sat},4}^{1/4} \left(\frac{\lambda}{\epsilon} \right)_8^{-7/20} \text{ keV}, \quad (3)$$

where r_{ph} can be obtained by setting the Thomson scattering depth $\tau(r_{\text{ph}}) = 1$, which gives $r_{\text{ph}} = 3.0 \times 10^9 L_{\text{sd},50}^{3/5} \Gamma_{\text{sat},4}^{-1} (\lambda/\epsilon)_8^{2/5}$ cm (Beniamini & Giannios 2017).

Furthermore, in order to obtain the synchrotron spectrum, we need to calculate the relevant break frequencies. The acceleration timescale due to magnetic reconnection is $t_{\text{acc}} = (\gamma_e m_e c^2) / (q\epsilon B')$ (Giannios 2010), where q is the electron charge and B' is the comoving magnetic field strength of the wind, while the synchrotron cooling timescale is $t_{\text{syn}} = (6\pi m_e c) / (\sigma_T B'^2 \gamma_e)$, where σ_T is the Thomson scattering cross-section. Thus, letting $t_{\text{acc}} = t_{\text{syn}}$ gives the maximum Lorentz factor of electrons,

$$\gamma_{\text{max}} = \left(\frac{6\pi q\epsilon}{\sigma_T B'} \right)^{1/2}. \quad (4)$$

Correspondingly, the maximum synchrotron frequency in the observer's rest-frame is

$$\nu_{\text{max}} = \frac{1}{1+z} \Gamma \gamma_{\text{max}}^2 \frac{qB'}{2\pi m_e c}. \quad (5)$$

The minimum Lorentz factor γ_m depends on the spectrum of electrons. PIC simulations suggest that the accelerated electrons, through reconnection, could have a power-law distribution with an index p (Sironi & Spitkovsky 2014; Guo et al. 2015; Kagan et al. 2015; Werner et al. 2016), where $p = 4\sigma^{-0.3}$ is adopted in accordance with previous numerical results, where σ is the magnetization parameter. If $p < 2$, we can simply assume $\gamma_m \simeq 1$. For $p > 2$, the minimum Lorentz factor is (Beniamini & Giannios 2017)

$$\gamma_m = \frac{p-2}{p-1} \frac{\epsilon_e}{2\xi} \sigma(r) \frac{m_p}{m_e}, \quad (6)$$

³ Note that the coefficient and indexes derived in Equation (3) are different from those of Beniamini & Giannios (2017).

where $\epsilon_e \sim 0.2$ is the fraction of the dissipated energy per electron and $\xi \simeq 0.2$ is the fraction of the electrons accelerated in the reconnection sites (Sironi et al. 2015). The typical synchrotron frequency is then

$$\nu_m = \frac{1}{1+z} \Gamma \gamma_m^2 \frac{qB'}{2\pi m_e c}. \quad (7)$$

In addition, the cooling frequency is (Sari et al. 1998)

$$\nu_c = \frac{1}{1+z} \frac{72\pi e m_e c^3 \Gamma^3}{\sigma_T B'^3 r^2}. \quad (8)$$

Letting $\nu_m = \nu_c$, we can obtain the radius r_{tr} at which the transition from fast cooling to slow cooling happens.

For $r_{\text{ph}} < r \leq r_{\text{tr}}$ and no synchrotron self-absorption (SSA), the electrons are in the fast-cooling regime for which the spectrum is (Sari et al. 1998)

$$L_\nu^{\text{syn}} = \begin{cases} L_{\nu, \text{max}}^{\text{syn}} (\nu/\nu_c)^{1/3} & \text{if } \nu < \nu_c, \\ L_{\nu, \text{max}}^{\text{syn}} (\nu/\nu_c)^{-1/2} & \text{if } \nu_c < \nu < \nu_m, \\ L_{\nu, \text{max}}^{\text{syn}} (\nu_m/\nu_c)^{-1/2} (\nu/\nu_m)^{-p/2} & \text{if } \nu_m < \nu < \nu_{\text{max}}, \end{cases} \quad (9)$$

where

$$L_{\nu, \text{max}}^{\text{syn}} = (1+z) \frac{m_e c^2 \sigma_T \Gamma B' N_e(r)}{3q}, \quad (10)$$

with $N_e(r)$ being the total number of emitting electrons in the wind at r . For $r_{\text{tr}} \leq r \leq r_{\text{sat}}$, the electrons turn into the slow-cooling regime and the spectrum becomes (Sari et al. 1998)

$$L_\nu^{\text{syn}} = \begin{cases} L_{\nu, \text{max}}^{\text{syn}} (\nu/\nu_m)^{1/3} & \text{if } \nu < \nu_m, \\ L_{\nu, \text{max}}^{\text{syn}} (\nu/\nu_m)^{-(p-1)/2} & \text{if } \nu_m < \nu < \nu_c, \\ L_{\nu, \text{max}}^{\text{syn}} (\nu_c/\nu_m)^{-(p-1)/2} (\nu/\nu_c)^{-p/2} & \text{if } \nu_c < \nu < \nu_{\text{max}}. \end{cases} \quad (11)$$

However, the SSA effect might play a role, and its frequency ν_a and corresponding electron Lorentz factor γ_a satisfy

$$\frac{2\nu_a^2}{c^2} \gamma_a \Gamma m_e c^2 \frac{\pi r^2}{\Gamma^2} = \frac{L_{\nu_a}^{\text{syn}}}{(1+z)^3}, \quad (12)$$

where

$$\nu_a = \frac{1}{1+z} \Gamma \gamma_a^2 \frac{qB'}{2\pi m_e c}. \quad (13)$$

At r_{ph} , usually $\nu_a > \nu_c$, and then at a radius r_{cr} , ν_a crosses ν_c . Since the spectrum below ν_a is $L_\nu \propto \nu^{11/8}$ (Granot & Sari 2002), the whole synchrotron spectrum can be written as follows. Initially, for $r_{\text{ph}} < r \leq r_{\text{cr}}$,

$$L_\nu^{\text{syn}} = \begin{cases} L_{\nu_a}^{\text{syn}} (\nu/\nu_a)^{11/8} & \text{if } \nu < \nu_a, \\ L_{\nu_a}^{\text{syn}} (\nu/\nu_a)^{-1/2} & \text{if } \nu_a < \nu < \nu_m, \\ L_{\nu_a}^{\text{syn}} (\nu_m/\nu_a)^{-1/2} (\nu/\nu_m)^{-p/2} & \text{if } \nu_m < \nu < \nu_{\text{max}}. \end{cases} \quad (14)$$

Furthermore, for $r_{\text{cr}} \leq r \leq r_{\text{tr}}$,

$$L_\nu^{\text{syn}} = \begin{cases} L_{\nu_a}^{\text{syn}} (\nu/\nu_a)^{11/8} & \text{if } \nu < \nu_a, \\ L_{\nu_a}^{\text{syn}} (\nu/\nu_a)^{1/3} & \text{if } \nu_a < \nu < \nu_c, \\ L_{\nu_a}^{\text{syn}} (\nu_c/\nu_a)^{1/3} \times (\nu/\nu_c)^{-1/2} & \text{if } \nu_c < \nu < \nu_m, \\ L_{\nu_a}^{\text{syn}} (\nu_c/\nu_a)^{1/3} \times (\nu_m/\nu_c)^{-1/2} (\nu/\nu_m)^{-p/2} & \text{if } \nu_m < \nu < \nu_{\text{max}}. \end{cases} \quad (15)$$

Lastly, for $r_{\text{tr}} \leq r \leq r_{\text{sat}}$,

$$L_\nu^{\text{syn}} = \begin{cases} L_{\nu_a}^{\text{syn}} (\nu/\nu_a)^{11/8} & \text{if } \nu < \nu_a, \\ L_{\nu_a}^{\text{syn}} (\nu/\nu_a)^{1/3} & \text{if } \nu_a < \nu < \nu_m, \\ L_{\nu_a}^{\text{syn}} (\nu_m/\nu_a)^{1/3} \times (\nu/\nu_m)^{-(p-1)/2} & \text{if } \nu_m < \nu < \nu_c, \\ L_{\nu_a}^{\text{syn}} (\nu_m/\nu_a)^{1/3} \times (\nu_c/\nu_m)^{-(p-1)/2} (\nu/\nu_c)^{-p/2} & \text{if } \nu_c < \nu < \nu_{\text{max}}. \end{cases} \quad (16)$$

The non-thermal synchrotron spectrum can be obtained by integrating the above expressions from the photospheric radius to the saturation radius. Now we can plot in Figure 1 the radiation spectrum of the pulsar wind, assuming the spin period $P = 5$ ms and the surface magnetic field strength $B_s = 10^{14}$ G. The distance in our calculations has been implicitly assumed to be at redshift $z = 0.193$, which corresponds to a luminosity distance of 972 Mpc. For different parameter sets, different cases are named in the form of ‘‘PxBs y ’’, with x denoting the spin period in ms and y denoting the logarithm of the magnetic field strength in Gauss, where we are discussing the P5Bs14 case. The spin-down luminosity is then

$$L_{\text{sd}} = L_0 \left(1 + \frac{t}{T_{\text{sd}}}\right)^{-2}, \quad (17)$$

where the present spin-down timescale $T_{\text{sd}} = 2 \times 10^3 I_{45} B_{s,15}^{-2} P_{-3}^2 R_6^{-6}$ s with I being the moment of inertia and R being the stellar radius, so that $t < T_{\text{sd}}$ and $L_{\text{sd}} \simeq L_0 = 3.8 \times 10^{49} B_{s,15}^2 P_{-3}^{-4} R_6^6$ ergs s^{-1} is a good approximation. The total spectrum (solid line) in Figure 1 consists of thermal (dotted line) and non-thermal (dashed line) components, and black upper limits are given by high-energy observations. We can see that the X-ray observations give the tightest constraint. Note that P5Bs14 is a nominal parameter set. If more optimistic parameters (e.g. P1Bs15) are taken, the X-ray flux of the wind is higher than the upper limit shown in Figure 1, so the X-ray emission should be detected by *XMM-Newton/Chandra*. In other words, the IGMD model will potentially be tested if a high-energy counterpart to any FRB is detected in the future.

The efficiency of converting the spin-down luminosity to the X-ray emission observed by *XMM-Newton/Chandra* can be calculated by

$$\eta_X \equiv \frac{\int_{0.5 \text{ keV}}^{6 \text{ keV}} (L_\nu^{\text{ph}} + L_\nu^{\text{syn}}) d\nu}{L_{\text{sd}}}. \quad (18)$$

For the P5Bs14 case here, we find $\eta_X = 4.7 \times 10^{-4}$.

3. CONSTRAINING PULSAR PARAMETERS

In order to be consistent with the upper limits given by *XMM-Newton/Chandra*, a solid requirement could be written as

$$\eta_X L_{\text{sd}} \lesssim L_{X, \text{lim}}, \quad (19)$$

where $L_{X, \text{lim}}$ is given by the observations (assuming $z = 0.193$). Therefore, we need to find a relationship between the X-ray efficiency and the spin-down luminosity. We choose three different spin periods ($P = 1, 3$ and 5 ms) and three different field strengths ($B_s = 10^{14}, 10^{15}$, and 10^{16} G), so that there are nine cases. The nine efficiencies

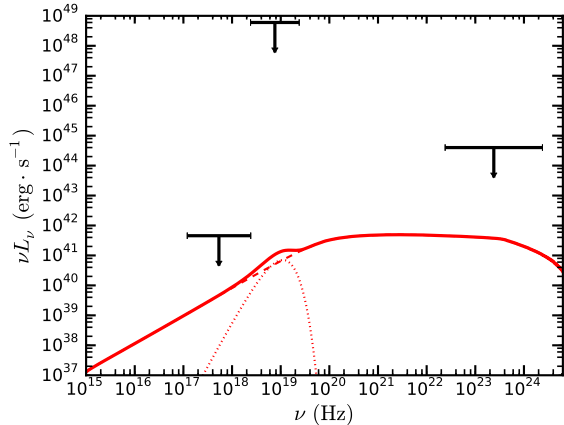


FIG. 1.— Radiation spectrum of a pulsar wind with internal gradual magnetic energy dissipation, assuming a spin period $P = 5$ ms and surface magnetic field strength $B_s = 10^{14}$ G. The total spectrum is represented by the solid line, which consists of the thermal component (dotted line) and the synchrotron emission (dashed line). Three upper limits in black are given by *XMM-Newton/Chandra*, *Fermi-GBM* and *Fermi-LAT* respectively.

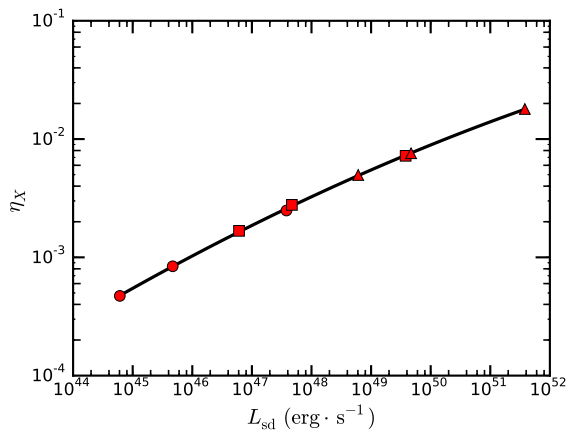


FIG. 2.— Dependence of η_X on the spin-down luminosity L_{sd} . Different symbols are used to differentiate the surface magnetic field strength: circles, squares and triangles are for $B_s = 10^{14}$, 10^{15} and 10^{16} G respectively.

are obtained in the same way as described in the previous section. In Figure 2 we plot the dependence of η_X on L_{sd} and fit it with a polynomial. The best fit is expressed as

$$\log \eta_X = -0.007794(\log L_{sd})^2 + 0.9829 \log L_{sd} - 31.71. \quad (20)$$

Substituting into the requirement (19), we can get the critical spin-down luminosity $L_{sd,cr} = 8.68 \times 10^{44}$ erg s $^{-1}$, which is obtained by letting $\eta_X L_{sd} = L_{X,lim}$. Therefore, the requirement $L_{sd} < L_{sd,cr}$ gives a constraint on the spin period and field strength of the pulsar, which is shown in Figure 3. The parameter space below the solid line is excluded by the observations.

We next consider the effect of the wind's saturation

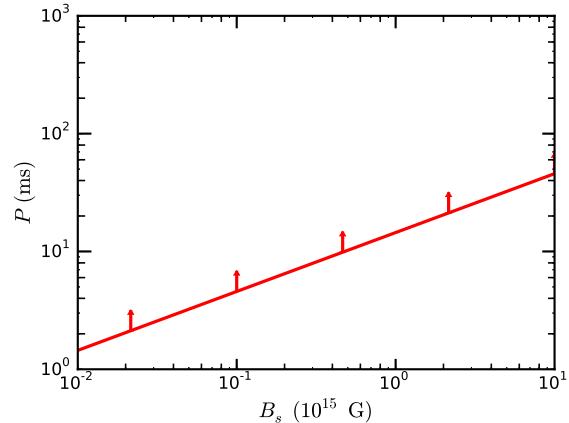


FIG. 3.— Constraint on the spin period and surface magnetic field strength of a pulsar obtained from the requirement (19). The reasonable parameter space lies above the solid line.

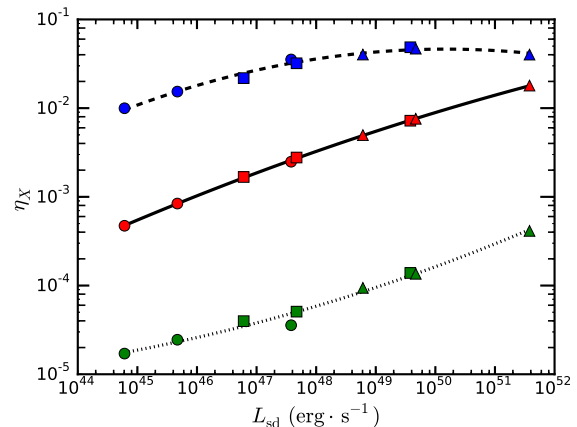


FIG. 4.— Influence of different Γ_{sat} on the dependence of η_X on L_{sd} . The solid line is the same as in Figure 2, while the dashed line is for $\Gamma_{sat} = 10^3$ and the dotted line is for $\Gamma_{sat} = 10^5$.

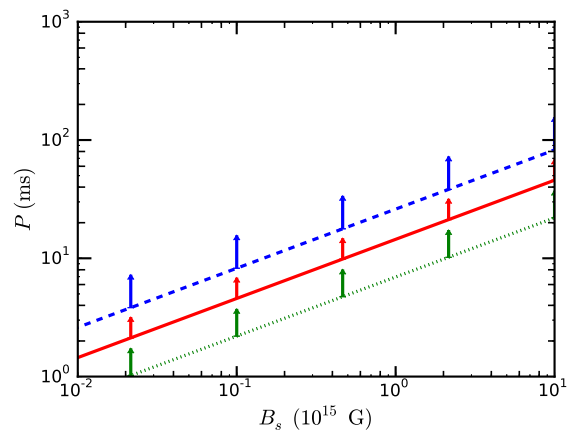


FIG. 5.— Three constraints obtained for three values of Γ_{sat} . The red solid line is the same as in Figure 3, while the blue dashed line is for $\Gamma_{sat} = 10^3$ and the green dotted line is for $\Gamma_{sat} = 10^5$.

Lorentz factor (Γ_{sat}) on the efficiency. To our knowledge, the saturation Lorentz factor Γ_{sat} depends on the initial magnetization parameter (σ_0) in the form of $\Gamma_{\text{sat}} = \sigma_0^{3/2}$ (Drenkhahn 2002; Drenkhahn & Spruit 2002; Giannios & Spruit 2005; Beniamini & Giannios 2017). For a Poynting-flux-dominated outflow, the efficiency of converting magnetic energy to radiation is expected to rely on the magnetization parameter. This issue is worth investigating from a theoretical point of view, since it will help study the properties of a Poynting-flux-dominated outflow and then reveal the mystery of a central engine. In addition to the canonical $\Gamma_{\text{sat}} = 10^4$ assumed above, here we choose the other two values of 10^3 and 10^5 and thus new efficiencies are obtained. Strong dependence of η_X on Γ_{sat} is shown in Figure 4, implying that lower magnetized outflows are more efficient at converting magnetic energy to radiation. The critical spin-down luminosities in the cases of $\Gamma_{\text{sat}} = 10^3$ and 10^5 are $L_{\text{sd,cr}} = 8.24 \times 10^{43}$ and $1.63 \times 10^{46} \text{ erg s}^{-1}$ respectively, and the corresponding constraints on P and B_s are shown in Figure 5. It is the $\Gamma_{\text{sat}} = 10^3$ case that places the most stringent constraint on the pulsar parameters.

4. CONCLUSIONS AND DISCUSSION

In this work we have assumed a rapidly rotating highly magnetized pulsar as the origin of FRB 121102 and constrained its spin period and magnetic field strength with upper limits given by current multi-wavelength observations. The magnetic energy dissipation in an isotropic pulsar wind should produce notable emission in the X-ray band. The non-detection by *XMM-Newton/Chandra* implies that the spin-down luminosity should be less than a critical value $L_{\text{sd,cr}}$. We derived the efficiency of converting the spin-down luminosity to X-ray luminosity (η_X) and obtained its dependence on L_{sd} . This efficiency depends strongly on the saturation Lorentz factor of the wind, or more intrinsically speaking, on the initial magnetization parameter of the wind. Outflows with a higher magnetization convert less energy to radiation. The reason for this is that the synchrotron emission turns from the fast-cooling regime to the slow-cooling regime as σ_0 increases, which is consistent with the conclusion by Beniamini & Giannios (2017). Thus, for the three cases considered in this work, it is the $\Gamma_{\text{sat}} = 10^3$ case gives the most stringent constraint on the pulsar parameters. The method of using high-energy data to constrain some of the model parameters is relevant for newborn pulsars with ages younger than T_{sd} , which is not the case for any known Galactic magnetar (Tendulkar et al. 2016)⁴. Also, the IGMD model is not easily tested with the current observations of pulsar wind nebulae (PWNe)⁵. However, it will be testable with observations of GRBs or SLSNe,

⁴ Note that very bright, high-energy emission from internal magnetic dissipation in the wind cannot last for a very long time. In fact, its luminosity will decay significantly after the initial spin-down timescale of a newborn rapidly rotating highly magnetized pulsar. At later times, an additional dominant emission could arise from an interaction of the wind with its ambient medium or supernova ejecta (for reviews see Gaensler & Slane 2006; Slane 2017).

⁵ Actually, we have compared the IGMD model to observations of the present Crab nebula by taking the parameters of the Crab pulsar. With a distance of 2.2 kpc, $B_s = 4 \times 10^{12}$ G, and $P = 33$ ms, the predicted flux ($\sim 10^{-11} \text{ erg cm}^{-2} \text{ s}^{-1}$ at 5 keV) of the high-energy emission from internal magnetic dissipation

which are driven by newborn millisecond magnetars. In particular, this model will be possibly tested if the association of an FRB with a GRB or an SLSN is detected in the future.

We note that several works have placed limits on the pulsar scenario, but most of these limits were obtained from the observations of the persistent radio counterpart to FRB 121102. For instance, Kashiyama & Murase (2017) studied the emission from a PWN in the framework of the “burst-in-bubble” model (Murase et al. 2016). With its application to the quasi-steady radio counterpart, they constrained the spin period and the magnetic field strength of the young pulsar by the minimum energy requirement for the PWN. The model in Dai et al. (2017) differs from Kashiyama & Murase (2017) in a way that they considered a PWN without surrounding supernova ejecta and thus new constraints on the wind luminosity and the ambient medium density were obtained. Moreover, the age of the pulsar can be constrained by radio observations (Beloborodov 2017; Metzger et al. 2017) and by other fair arguments like dispersion measures (Cao et al. 2017; Kashiyama & Murase 2017). Lyutikov (2017) argued that the energy source for FRB 121102 can also be constrained. In our paper, we focus on the X-ray-to-gamma-ray follow-up observations of FRB 121102 and our new constraints on P and B_s are generally consistent with previous works (Cao et al. 2017; Dai et al. 2017; Kashiyama & Murase 2017; Lyutikov 2017).

The difference between our work and Zhang & Zhang (2017) lies not only in the selected upper limits, but also in the methods of calculation. Instead of simply assuming a constant radiation efficiency, we start from the realistic IGMD model of a pulsar wind and the efficiency is obtained in a more physical way. Determining the radiation efficiency has been a key issue for the Poynting-flux-dominated outflow in the previous studies, especially in the GRB field (e.g. Beniamini et al. 2015, 2016; Beniamini & Giannios 2017). The method we developed in this work could be applied to various situations, and constraining the parameters of the pulsar origin of FRB 121102 is just one of them. More comprehensive work could be done with our method, such as applying it to short GRBs, magnetar giant flares, and even some black-hole accreting systems. These studies will appear elsewhere.

We thank Yun-Wei Yu, Bing Zhang, and an anonymous referee for helpful comments. This work was supported by the National Basic Research Program of China (973 Program grant 2014CB845800) and the National Natural Science Foundation of China grant 11573014.

is far below the observed X-ray-to-gamma-ray flux of the Crab nebula ($\sim 10^{-8} \text{ erg cm}^{-2} \text{ s}^{-1}$ at 5 keV; for a recent review see Bühler & Blandford 2014). Therefore, the observed X-ray flux of the Crab nebula is dominated by the emission from shocks (in particular, a terminative reverse shock) produced by an interaction of the pulsar wind with its ambient gas.

REFERENCES

- Atoyan, A. M. 1999, *A&A*, 346, L49
- Bagchi, M. 2017, *ApJ*, 838, L16
- Bassa, C. G., Tendulkar, S. P., Adams, E. A. K., et al. 2017, *ApJ*, 843, L8
- Beloborodov, A. M. 2017, *ApJ*, 843, L26
- Beniamini, P. 2014, *MNRAS*, 445, 3892
- Beniamini, P., Nava, L., Duran, R. B., & Piran, T. 2015, *MNRAS*, 454, 1073
- Beniamini, P., Nava, L., & Piran, T. 2016, *MNRAS*, 461, 51
- Beniamini, P., & Giannios, D. 2017, *MNRAS*, 468, 3202
- Bühler, R., & Blandford, R. D. 2014, *Rep. Prog. Phys.*, 77, 066901
- Burke-Spolaor, S., & Bannister, K. W. 2014, *ApJ*, 792, 19
- Caleb, M. et al. 2017, *MNRAS*, 468, 3746
- Cao, X. F., Yu, Y. W., & Dai, Z. G. 2017, *ApJ*, 839, L20
- Champion, D. J., Petroff, E., Kramer, M., et al. 2015, *MNRAS*, 460, L30
- Chatterjee, S., Law, C. J., Wharton, R. S., et al. 2017, *Nature*, 541, 58
- Ciolfi, R., & Siegel, D. M. 2015, *ApJ*, 798, L36
- Connor, L., Sievers, J., & Pen, U.-L. 2016, *MNRAS*, 458, L19
- Cordes, J. M., & Wasserman, I. 2016, *MNRAS*, 457, 232
- Coroniti, F. V. 1990, *ApJ*, 349, 538
- Dai, Z. G. 2004, *ApJ*, 606, 1000
- Dai, Z. G., & Lu, T. 1998a, *A&A*, 333, L87
- Dai, Z. G., & Lu, T. 1998b, *Phys. Rev. Lett.*, 81, 4301
- Dai, Z. G., Wang, J. S., Wu, X. F., & Huang, Y. F. 2016, *ApJ*, 829, 27
- Dai, Z. G., Wang, J. S., & Yu, Y. W. 2017, *ApJ*, 838, L7
- Drenkhahn, G. 2002, *A&A*, 387, 714
- Drenkhahn, G., & Spruit, H. C. 2002, *A&A*, 391, 1141
- Falcke, H., & Rezzolla, L. 2014, *A&A*, 562, 137
- Gaensler, B. M., & Slane, P. O. 2006, *ARA&A*, 44, 17
- Giannios, D., & Spruit, H. C. 2005, *A&A*, 430, 1
- Giannios, D. 2006, *A&A*, 457, 763
- Giannios, D. 2008, *A&A*, 480, 305
- Giannios, D. 2010, *MNRAS*, 408, L46
- Giannios, D. 2012, *MNRAS*, 422, 3092
- Granot, J., & Sari, R. 2002, *ApJ*, 568, 820
- Gu, W. M., Dong, Y. Z., Liu, T., Ma, R., & Wang, J. 2016, *ApJ*, 823, L28
- Guo, F., Liu, Y. H., Daughton, W., & Li, H. 2015, *ApJ*, 806, 167
- Kagan, D., Sironi, L., Cerutti, B., & Giannios, D. 2015, *Space Sci. Rev.*, 191, 545
- Kashiyama, K., Ioka, K., & Mészáros, P. 2013, *ApJ*, 776, L39
- Kashiyama, K., & Murase, K. 2017, *ApJ*, 839, L3
- Katz, J. I. 2016a, *MPLA*, 31, 1630013
- Katz, J. I. 2016b, *ApJ*, 826, 226
- Katz, J. I. 2017a, *MNRAS*, 469, L39
- Katz, J. I. 2017b, *MNRAS*, 467, L96
- Keane, E. F., Stappers, B. W., Kramer, M., & Lyne, A. G. 2012, *MNRAS*, 425, L71
- Keane, E. F., Johnston, S., Bhandari, S., et al. 2016, *Nature*, 530, 453
- Kulkarni, S. R., Ofek, E. O., Neill, J. D., Zheng, Z., & Juric, M. 2014, *ApJ*, 797, 70
- Liu, T., Romero, G. E., Liu, M.-L., & Li, A. 2016, *ApJ*, 826, 82
- Liu, Y. H., Guo, F., Daughton, W., Li, H., & Hesse, M. 2015, *Phys. Rev. Lett.*, 114, 095002
- Lorimer, D. R., Bailes, M., McLaughlin, M. A., Narkevic, D. J., & Crawford, F. 2007, *Science*, 318, 777
- Lyubarsky, Y. E. 2005, *MNRAS*, 358, 113
- Lyutikov, M. 2017, *ApJ*, 838, L13
- Lyutikov, M., Burzawa, L., & Popov, S. B. 2016, *MNRAS*, 462, 94
- Marcote, B., Paragi, Z., Hessels, J. W. T., et al. 2017, *ApJ*, 834, L8
- Masui, K., Lin, H.-H., Sievers, J., et al. 2015, *Nature*, 528, 523
- Metzger, B. D., Giannios, D., Thompson, T. A., Bucciantini, N., & Quataert, E. 2011, *MNRAS*, 413, 2031
- Metzger, B. D., Berger, E., & Margalit, B. 2017, *ApJ*, 841, 14
- Murase, K., Kashiyama, K., & Mészáros, P. 2016, *MNRAS*, 461, 1498
- Petroff, E., Bailes, M., Barr, E. D., et al. 2015, *MNRAS*, 447, 246
- Popov, S. B., & Postnov, K. A. 2013, *arXiv:1307.4924*
- Ravi, V., Shannon, R. M., & Jameson, A. 2015, *ApJ*, 799, L5
- Ravi, V., Shannon, R. M., Bailes, M., et al. 2016, *Science*, 354, 1249
- Rezzolla, L., & Kumar, P. 2015, *ApJ*, 802, 95
- Sari, R., Piran, T., Narayan, R. 1998, *ApJ*, 497, L17
- Scholz, P., Spitler, L. G., Hessels, J. W. T., et al. 2016, *ApJ*, 833, 177
- Scholz, P., Bogdanov, S., Hessels, J. W. T., et al. 2017, *arXiv:1705.07824*
- Sironi, L., & Spitkovsky, A. 2014, *ApJ*, 783, L21
- Sironi, L., Petropoulou, M., & Giannios, D. 2015, *MNRAS*, 450, 183
- Spitler, L. G., Cordes, J. M., Hessels, J. W. T., et al. 2014, *ApJ*, 790, 101
- Spitler, L. G., Scholz, P., Hessels, J. W. T., et al. 2016, *Nature*, 531, 202
- Spruit, H. C., Daigne, F., & Drenkhahn, G. 2001, *A&A*, 369, 694
- Slane, P. O. 2017, *arXiv:1703.09311v1*
- Tendulkar, S. P., Kaspi, V. M., & Patel, C. 2016, *ApJ*, 827, 59
- Tendulkar, S. P., Bassa, C. G., Cordes, J. M., et al. 2017, *ApJ*, 834, L7
- Thornton, D., Stappers, B., Bailes, M., et al. 2013, *Science*, 341, 53
- Totani, T. 2013, *PASJ*, 65, L12
- Wang, J. S., Yang, Y. P., Wu, X. F., Dai, Z. G., & Wang, F. Y. 2016, *ApJ*, 822, L7
- Werner, G. R., Uzdensky, D. A., Cerutti, B., Nalewajko, K., & Begelman, M. C. 2016, *ApJ*, 816, L8
- Xi, S. Q., Tam, P. T., Peng, F. K., & Wang, X. Y. 2017, *ApJ*, 842, L8
- Younes, G., Kouveliotou, C., Huppenkothen, D., et al. 2016, *ATel*, 8781, 1
- Zhang, B. 2014, *ApJ*, 780, L21
- Zhang, B. 2016, *ApJ*, 827, L31
- Zhang, B., & Yan, H. R. 2011, *ApJ*, 726, 90
- Zhang, B. B., & Zhang B. 2017, *ApJ*, 843, L13